J. Indian Inst. Sci., Sept.–Oct. 2000, **80**, 477–502.

IISc THESES ABSTRACTS

Thesis Abstract (Ph. D.)

Role of anions in modulating the structure, reactivity and bonding of Cu(I)–dppm (bis(diphenylphosphino)methane) complexes – An experimental and theoretical study by
Jitendra K. Bera
Research supervisor: Prof. A. G. Samuelson
Department: Inorganic and Physical Chemistry

1. Introduction

The use of diphosphines as ligands for transition metals continues to be a field of intense interest in both fundamental and applied chemistry. The ligand bis(diphenylphosphino)methane (dppm) is particularly well studied because of its ability to act as a bridging ligand between transition metals.[1] Cu(I) forms several di- and polynuclear complexes with dppm. The structure, nuclearity, bonding and reactivity of these complexes in the presence of different anions such as oxyanions, halides, etc. have been examined in this study.

2. Oxyanion encapsulated Cu(I)-dppm complexes

A Cu(I)-dppm dimeric complex $[Cu_2(dppm)_2(dmcn)_3](BF_4)_2$ (**1**) has been synthesized by treating the $[Cu(CH_3CN)_4]BF_4$ with dppm and excess dmcn (dmcn = dimethyl cyanamide). The dimeric structure of **1** with closely spaced copper centres, flanked by the phenyl rings of dppm ligands creates a cavity that is occupied by neutral dmcn in this complex. Several Cu(I)-dppm complexes containing different oxyanions have been prepared by treating **1** with the respective oxyanion salt. Independent synthesis of these complexes has also been accomplished by starting with the corresponding copper(II) salts. Cu(I)-dppm complexes encapsulating the ClO_4^-, NO_3^-, $PhCO_2^-$, SO_4^{2-} and WO_4^{2-} have been synthesized. The crystal and molecular structures of the complexes **1, 2, 4** and **7** have been established by single-crystal X-ray crystallography. The molecular structure of complex **2** unambiguously confirms the encapsulation of ClO_4^- inside the $Cu_2(dppm)_2$ core. The structure of the dimeric unit of **2** is similar to complex **1** except for the fact that the bridging dmcn ligand is replaced by the ClO_4^- anion.[2]

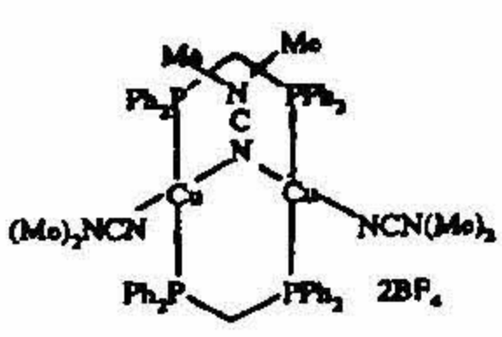

1

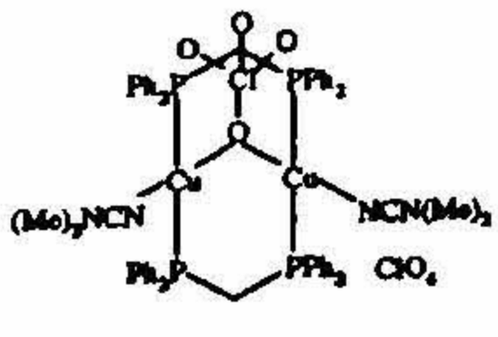

2

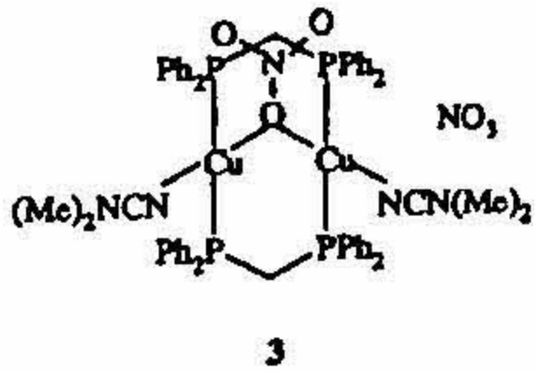

3

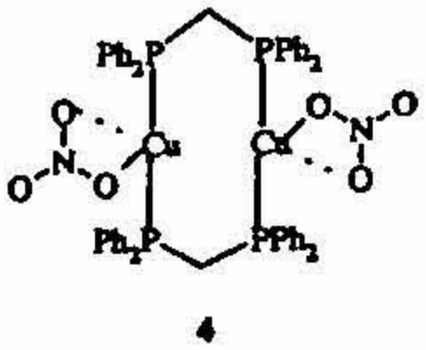

4

The composition of complexes **3** and **4** bring out some interesting features regarding the interaction of dmcn and NO_3^- with the $Cu_2(dppm)_2$ system: the labile nature of both NO_3^- and dmcn, which allows formation of either **3** or **4** depending on the ratio of the reagents used.

The coordination of benzoate and sulphate anion to copper has been established by IR spectroscopy of complexes **5** and **6**, respectively. Treatment of Na_2WO_4 with **1** leads to the formation of a trimeric complex **7**. The most interesting observation in this structure is that the WO_4^{2-} is located inside the cavity formed by the phenyl rings of the dppm ligand.

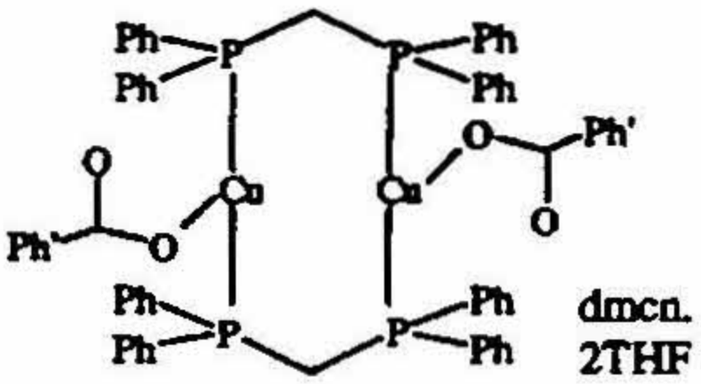

5 Ph' = Me-C_6H_4

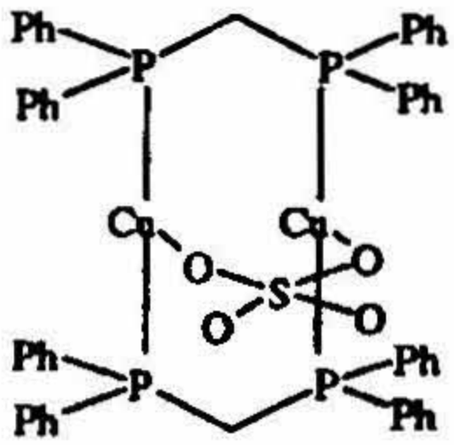

6a

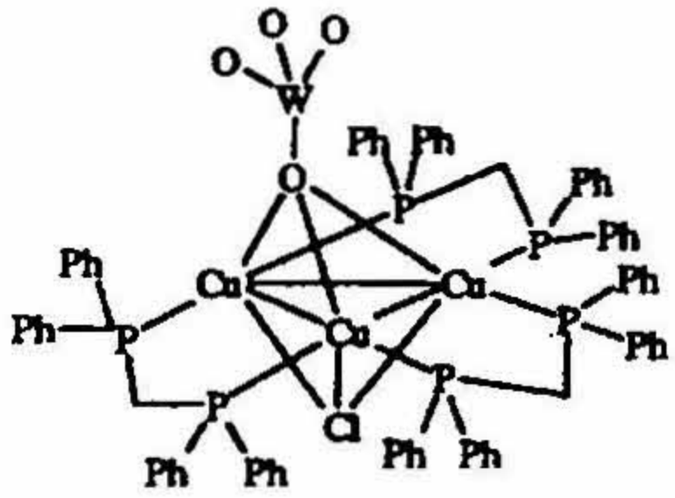

7

The short Cu–O distances found in these complexes clearly indicate that the encapsulation of oxyanion is primarily due to coordination to copper. Significantly, the noncovalent C–H···O interactions between the oxygen atoms of the oxyanion and the methylene and phenyl protons of the dppm ligands also play an important role in anchoring the guest inside the cavity. Several short CH···O distances are noted in the crystal structure of these complexes emphasizing the role of noncovalent interactions in the encapsulation.

The inclusion of the oxyanion inside the $Cu_2(dppm)_2$ core can be sensed by several spectroscopic techniques such as IR and ^1H and $^{31}P\{^1H\}$ NMR spectra. The ^{31}P chemical shift values of complexes **2, 3** and **5** indicate the relative order of the strength of interactions of oxyanions with Cu(I) in solution as $ClO_4^- < NO_3^- < PhCO_2^-$ in complete accordance with the trend in the solid state based on Cu-O distances. The association constants are 249 mol^{-1} dm^3 for ClO_4^- and 154 mol^{-1} dm^3 for NO_3^-. It is interesting to note that though NO_3^- causes a larger shift, ClO_4^- forms a thermodynamically more stable complex compared to the planar NO_3^-. The greater number of oxygen atoms allows many more C–H···O interactions and the tetrahedral disposition of the oxygen atoms make a better fit of the anion in the cavity.

3. Anion-controlled nuclearity and Cu...Cu distances in Cu(I)–dppm complexes

Addition of X (X is Cl^-, Br^- and I^-) to **1** or $Cu_2(dppm)_2(CH_3CN)_4(ClO_4)_2$ immediately leads to the formation of dicapped trimeric $Cu_3(dppm)_3$ complexes **8**, **9** and **10**, respectively. The molecular structure and the nuclearity of complexes **9** and **10** have been established by X-ray diffraction study. In all these trinuclear complexes, the three copper atoms form a triangle with a dppm ligand bridging each edge to form a Cu_3P_6 core. The dicapping halide ions are bonded to the three copper atoms in a μ_3 fashion from opposite sides of the triangle. A similar dicapped trinuclear complex $[Cu_3(dppm)_3(\mu_3\text{-}SC_6H_4\text{–}CH_3)_2]$ (ClO_4) (**12**) has also been synthesized.

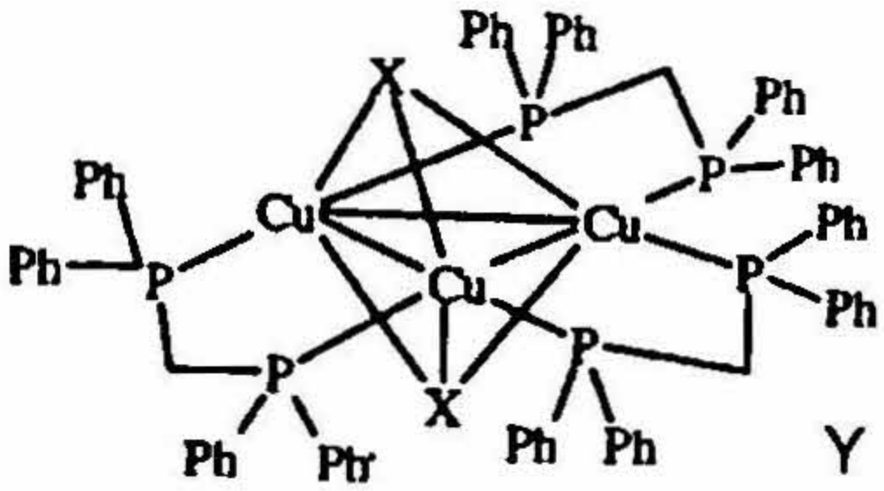

X = Cl, Y = ClO_4 (8)
X = Br, Y = ClO_4. 2THF (9)
X = I, Y = I. $2CH_2Cl_2$. CH_3OH (10)
X = $SC_6H_4CH_3$ Y = ClO_4 (12)

The conversion from trimeric $Cu_3(dppm)_3$ to dimeric $Cu_2(dppm)_2$ species has also been attempted in this study. Treatment of **1** with warm methanol gives a monocapped hydroxo complex $[Cu_3(dppm)_3(\mu_3\text{–}OH)](ClO_4)_2$. The trimeric $Cu_3(dppm)_3(\mu_3\text{–}OH)^{2+}$ on treatment with HBF_4 and dmcn converts to dimeric **1** at room temperature and is complete in 30 min. The conversion is not so facile when the capping ligands are Cl^-. Prolonged treatment of $[Cu_3(dppm)_3(\mu_3\text{-}Cl)_2]Cl$ with excess dmcn and subsequent crystallization gives the complex $[Cu_2(dppm)_2(dmcn)(Cl)_2]$.2dmcn (**11**).[3]

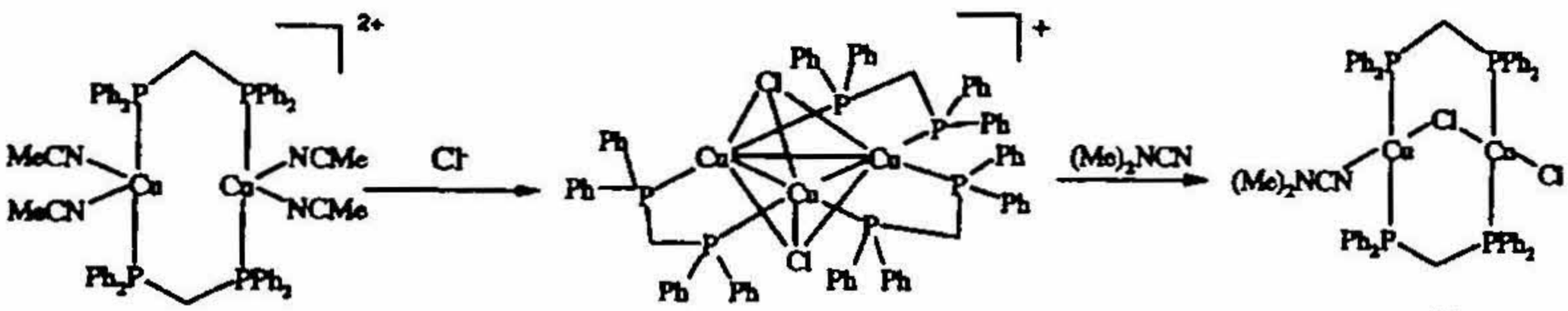

11

The Cu...Cu distances in these trimeric complexes are primarily controlled by the bite size of the dppm ligand. In a series of complexes containing dppm, the other bridging ligand plays an important role in fine-tuning the metal–metal distances. Among the dicapped halide complexes, the longest distances are observed for the Cl complex and the smallest for the Br complex, and the I complex has longer distances than the Br complex. The shortest Cu...Cu distances are observed in the dicapped acetylide complex $[Cu_3(dppm)_3(C \equiv CPh)_2](BF_4)$. In general, the presence of π donor (Cl^-) leads to longer distances and a π acceptor (HC_2^-) leads to shorter Cu...Cu distances.

In order to understand the distance variation in these complexes, an *ab initio* theoretical study has been undertaken on the model $Cu_3X_2^+$ systems (X = Cl, Br, HC_2). Detailed natural population analyses of these systems suggests that a filled π orbital such as in Cl^- increases the antibonding nature of the copper core *d* orbitals and lead to larger Cu...Cu distances. In the case of capping ligands that are larger such as Br^- or I^-, the filled π orbital repulsion is less due to more diffuse nature of their atomic orbitals. The superior overlap of the 4*s* and 4*p* orbitals of copper with the capping ligand in the Br complex leads to better Cu–Br bonding as well as shorter Cu...Cu distances. Capping ligands having π^* orbitals of suitable symmetry, such as acetylide, can reduce the antibonding nature of the filled *d*-manifold on the copper core and shorten the Cu...Cu distances.

The identification of the nuclearity of Cu(I)-dppm complexes has been attempted on the basis of solid-state emission spectra.

4. Anion-promoted reaction of $[Cu_3(dppm)_3(\mu_3\text{-}OH)](ClO_4)_2$ with heterocumelenes

To study the reactivity generated by mismatch of hard donor ligand and soft metal center, the reaction of $[Cu_3(dppm)_3(\mu_3\text{-}OH)](ClO_4)_2$ with CS_2, PhNCS and MeNCS has been carried out. Though complex **1** does not undergo any reaction, the lone pair of the oxygen atom in $[Cu_3(dppm)_3(\mu_3\text{-}OH)](ClO_4)_2$ attacks the carbon centre of the heterocumelenes and forms insertion products. In the case of PhNCS and MeNCS, such insertion products have been isolated. The intermediate formed in the reaction of $[Cu_3(dppm)_3(\mu_3\text{-}OH)](ClO_4)_2$ with CS_2 immediately converts to $Cu(dppms)_2ClO_4$ (**16**) (dppms = Ph_2P–CH_2–PPh_2 = S). The single-crystal X-ray diffraction study of **16** confirms that the dppm ligand has been oxidized to dppms.

5. Anion-modulated reactivity of Cu(III) species with soft ligands

Anion-modulated reactivity of Cu(III) centers with the soft ligands CO, C_2H_4 and C_2H_2 (L) has been probed by *ab-initio* methods. Calculations have been carried out on a number of Cu(III) units Cu^{3+}, HCu^{2+}, $HOCu^{2+}$, FCu^{2+}, OCu^{+} and NCu. The auxiliary groups, H^-, HO^- and F^- (X), have been chosen to model the effect of exclusively or predominantly σ type interactions with the metal. In addition, oxo and nitrido units have been employed to probe the consequences of more effective π donation. These groups also exhibit a large variation of charge on the metal and hence reveal the significance of electrostatic interactions in modulating various properties.

Natural bond orbital analyses on these species show that the charge on the copper atom in all the HOS species is substantially lower than 3. The ancillary ligand X is computed to carry a net positive charge in the dicationic complexes! The *d*-orbital occupancies of copper in all the complexes are considerably greater than 9!

Computed trends have been explained on the basis of the electronic structures of these complexes. In all the formally Cu(III) species, electron deficiency is mainly concentrated in the ancillary unit X. The electronic configuration on the Cu is close to d^{10} in all the systems. Ligand-to-metal σ donation is therefore relatively weak resulting in long Cu–X and Cu–C bonds. The higher interaction energies result mainly from electrostatic effects in these highly charged systems. The magnitude of π back donation is not significant in Cu(III) species with the exception of NCuCO. The computed properties of this system are remarkably similar to typical Cu(I) complexes.

Many of the key features of the electronic structures of carbonyl complexes are found to be common to C_2H_4 and C_2H_2 complexes. However, a subtle difference is noted. In the carbonyl complex, most of the deficiency is localized in the ancillary ligand X. In contrast, in the C_2H_4 and C_2H_2 complexes of Cu(III) with X as the ancillary ligand, electrons are removed from the organic fragment.[4]

6. Preference of Cu(I) for hard and soft ligands

In order to understand the preference of Cu(I) for different combinations of hard and soft ligands, the structure, energetics and electronic structures of $Cu(PH_3)_n(NH_3)_{4-n}^{+}$($n = 1$ to 4) have been analyzed. The results has been compared with isoelectronic $Ni(PH_3)_n(NH_3)_{4-n}$ and $Zn(PH_3)_n(NH_3)_{4-n}^{2+}$. The result shows that Ni(0) and Zn(II) stabilize with soft and hard donor ligands, respectively, while Cu(I) prefers a combination of both.

References

1. MORTON, D. A. V. AND ORPEN, A. G. — *J. Chem. Soc., Dalton Trans.*, 1992, 641 and references therein.
2. BERA, J. K., SAMUELSON, A. G. AND NETHAJI, M. — *Inorg. Chem.*, 1999, 38, 1725–1735.
3. BERA, J. K., SAMUELSON, A. G. AND NETHAJI, M. — *Inorg. Chem.*, 1999, 38, 218–228.
4. BERA, J. K., SAMUELSON, A. G. AND CHANDRASEKHAR, J. — *Organometallics*, 1998, 17, 4136–4145.

Thesis Abstract (Ph.D.)

Kinetic and thermodynamic study of a non-inactivating K^+ current in a gonadotroph cell-line by J. K. Tiwari
Research supervisor: Dr S. K. Sikdar
Department: Molecular Biophysics

1. Introduction

In order to understand the function of biological molecule it is important to know its structure, and ion channels are no exception. Ion channels belong to the class of integral membrane proteins. They allow passage of more than ten million ions per second with remarkable selectivity towards the permeant ion. Most sensitive and versatile technique for the study of ion channel is electrophysiology. Patch-clamp technique[1] can monitor the behaviour of a single ion channel *in vivo* and real time. The first detailed kinetic analysis of ion channel was reported by Hodgkin and Huxley.[2] They showed that the flow of K^+ and Na^+ across the membrane of axon was controlled by two separate mechanisms. Of the voltage-gated ion channels, K^+ channels are ubiquitous and often more than one type is present in the same cell.[3] They control action potential in neurons and play important role in various physiological processes of endocrine and exocrine cells.[4,5]

αT3-1 is a gonadotroph cell line. Its cell membrane contains a variety of ion channels. Separation of the K^+ channel subtypes in αT3-1 cells reveal the presence of a non-inactivating K^+ current with unique kinetic properties in the presence of low free intracellular Ca^{2+} concentrations. This non-inactivating K^+ current activated with simple exponential time course. The same kinetic model was tenable at all temperatures and potentials. Temperature and electrophysiology were used as biophysical tools to study the mechanism associated with the activation of this K^+ channel. The model proposed by Hill and Chen[6] was used for the thermodynamic analysis of channel. This report demonstrates that their model is applicable to the K^+ channel described here and consistent with the recent understanding of ion-channel structure in general.

2. Material and methods

Non-inactivating K^+ currents were recorded using EPC-7 patch-clamp amplifier and data were collected online into an IBM-compatible AT-286 computer using CED1401 A/D interface. The generation of pulse protocols and preliminary analysis was done using WCP software. Electrophysiological measurements were performed at 10–35°C with pipette solution containing

150 mM KCl, 2 mM $MgCl_2$. $6H_2O$, 5 mM HEPES and 1 mM EGTA (pH 7.35), and bath solution containing 90 mM KCl, 50 mM choline chloride, 1 mM EGTA, 2 mM $MgCl_2.6H_2O$, 2 mM $CoCl_2.6H_2O$, 5 mM HEPES, and 10 mM glucose (pH 7.4) (All Sigma Chemicals). For data analysis, K^+ currents were analyzed with a modified Hodgkin–Huxley (1952) equation:

$$I_K = a(1-\exp(-(t-0.2)/\tau_n))^x \quad (1)$$

where I_k is the potassium current, a amplitude, t time, τ_n time constant of activation and x is related to the number of independent identical transitions before the channel becomes conducting. Final analyses and curve fittings were performed on a CDC4360 computer using programs developed in our laboratory.

3. Results and discussion

3.1. *Non-inactivating K^+ current traces and activation kinetics*

The non-inactivating K^+ currents were studied by applying depolarizing pulses from +10 to +135 mV in steps of 9.7 mV from a holding potential of −10 mV. Activation of the currents

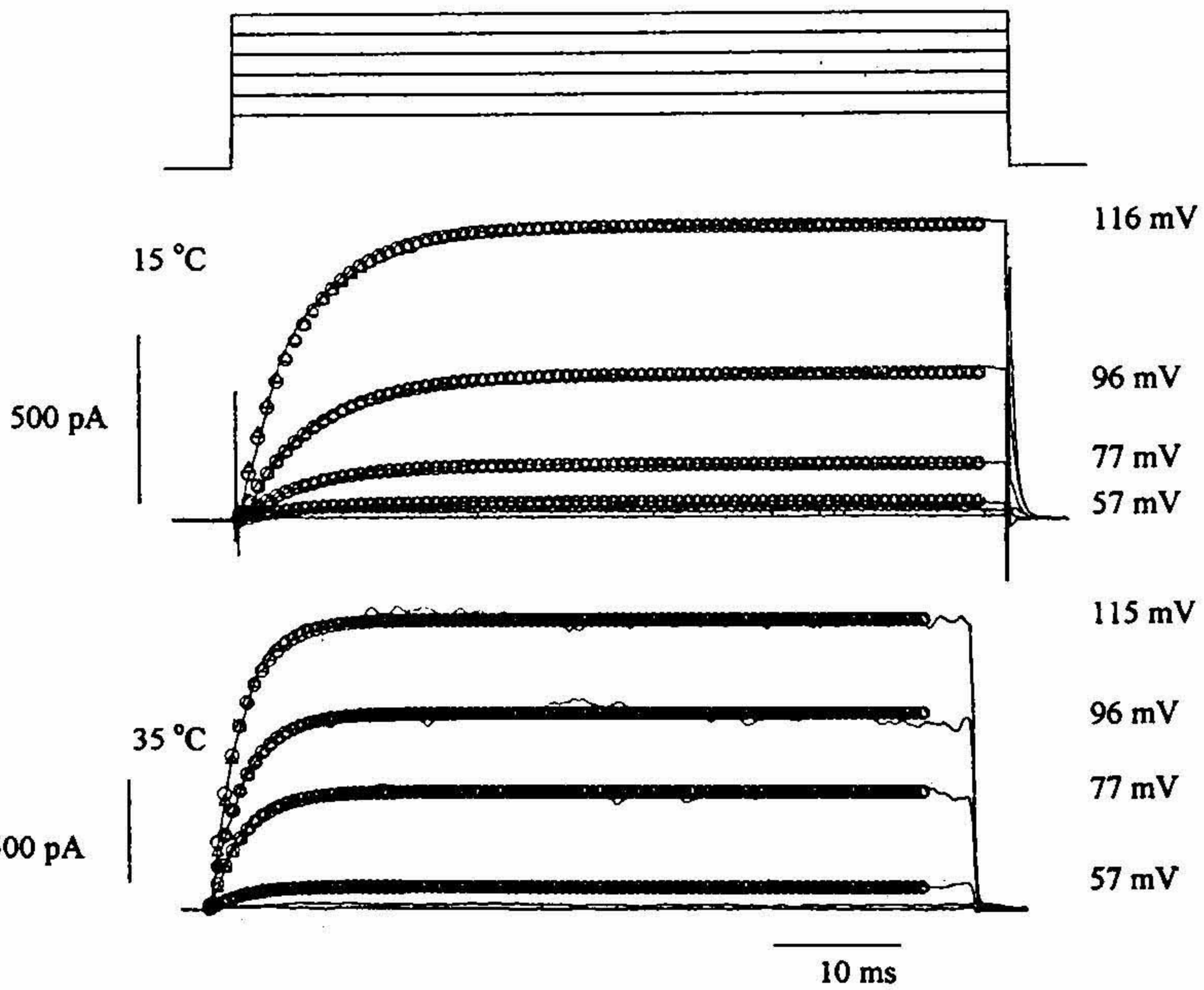

FIG. 1. Activation kinetics of non-inactivating K^+ current at 15 and 35°C. Representative whole cell currents from $V_{HOLD} = -10$ mV with fit using eqn (1), membrane voltage is indicated next to each trace. Activation time course of K^+ currents at two temperatures were fit with eqn (1) with $x = 1$ (triangle) and x as free parameter (circles). Current scale is shown on left and time scale is common. Fit has been shown with every tenth point plotted.

increased rapidly, both with greater depolarization and on increasing the bath temperature (Fig. 1). A mean leftward shift of about 4 mV per 10°C was observed in $V_{1/2}$ of activation with no obvious change in the slope or gating charge. The K^+ currents at different potentials and temperatures were analyzed with eqn (1). τ_n and x were floated to obtain the fit of the current traces and results were compared with value of x fixed to 1 (see Fig. 1). No significant difference was observed between the fits with $x = 1$ and x as a parameter, thus further analysis was done with $x = 1$. The exponential kinetics of the current was observed at all potentials (above +55 mV) and temperatures and was consistent with the two state model for channel activation.

The energy barrier for the transition between the closed and the open state was determined by studying the kinetics over a range of temperatures. The activation energies estimated from the Arrhenius plot for forward rate (α_n) were 46.16 and 34.73 kJ mol^{-1} and for backward rate (β_n) were 38.55 and 47.12 kJ mol^{-1} at 88 and 116 mV, respectively.

Effect of membrane potential on $\Delta G°$ was studied at 15° and 35°C. $\Delta G°$ was determined at various potentials using the equation

$$\ln(K_{eq}) = -\Delta G°/RT. \quad (2)$$

A striking feature of $\Delta G°$ is its quadratic variation with membrane potential and the curvature is prominent at 15°C (Fig. 3). $\Delta G°$, at each temperature, changes sign at potentials corresponding to the value where half the channels are in open state. Earlier studies have suggested that

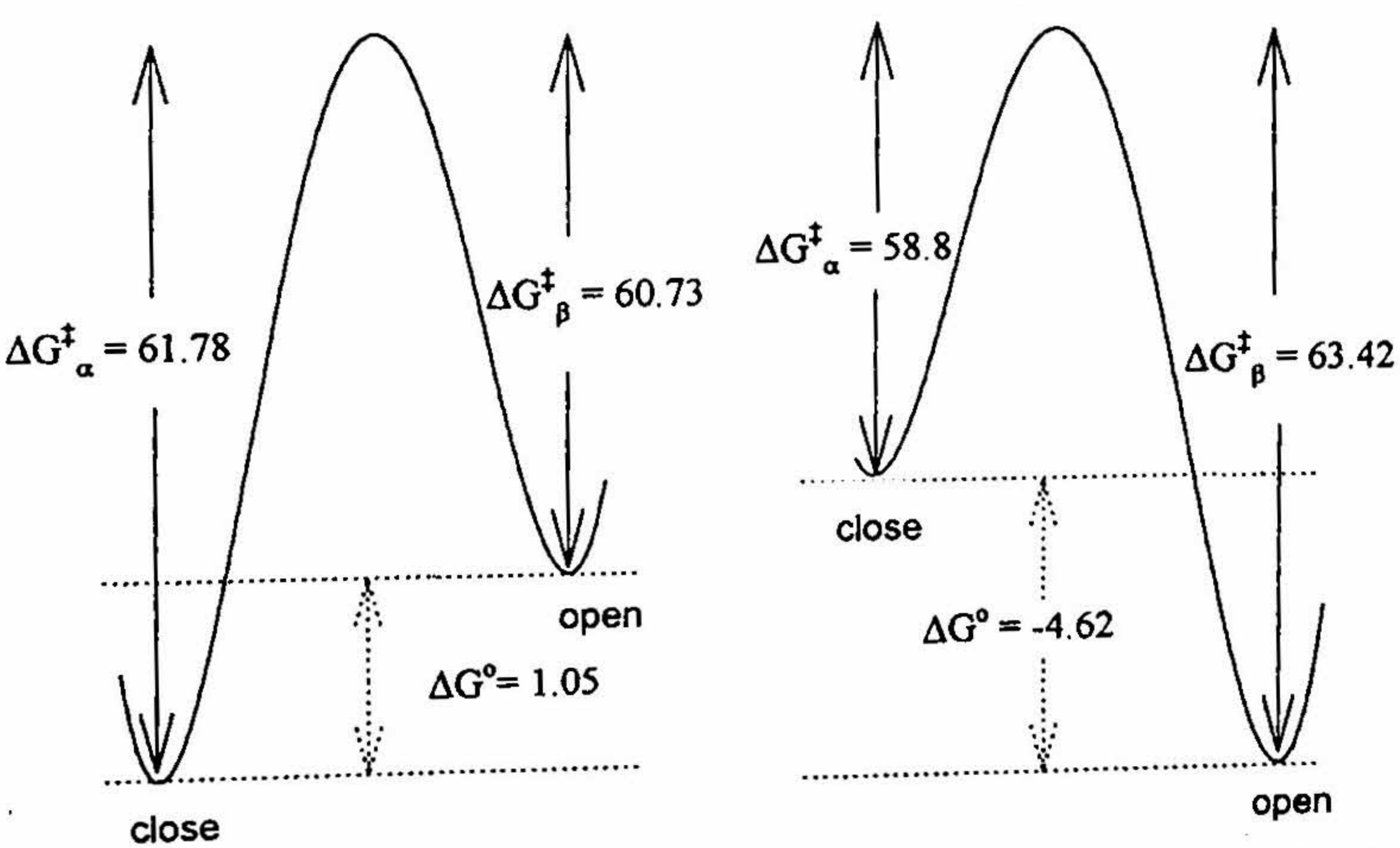

FIG. 2. Relative free energy of activation between open and closed configurations. The relative energy barrier from the two stable states (open and closed) of channel drawn for 88 and 116 mV. The change in free energy of activation was estimated by Arrhenius plot (not shown). The change in free energy ($\Delta G°$) between closed and open configurations was determined by difference in free energy of activation for α_n and β_n [i.e. $(\Delta G^{\ddagger}\alpha)$–$(\Delta G^{\ddagger}\beta)$] and is shown with dashed line for the two potentials.

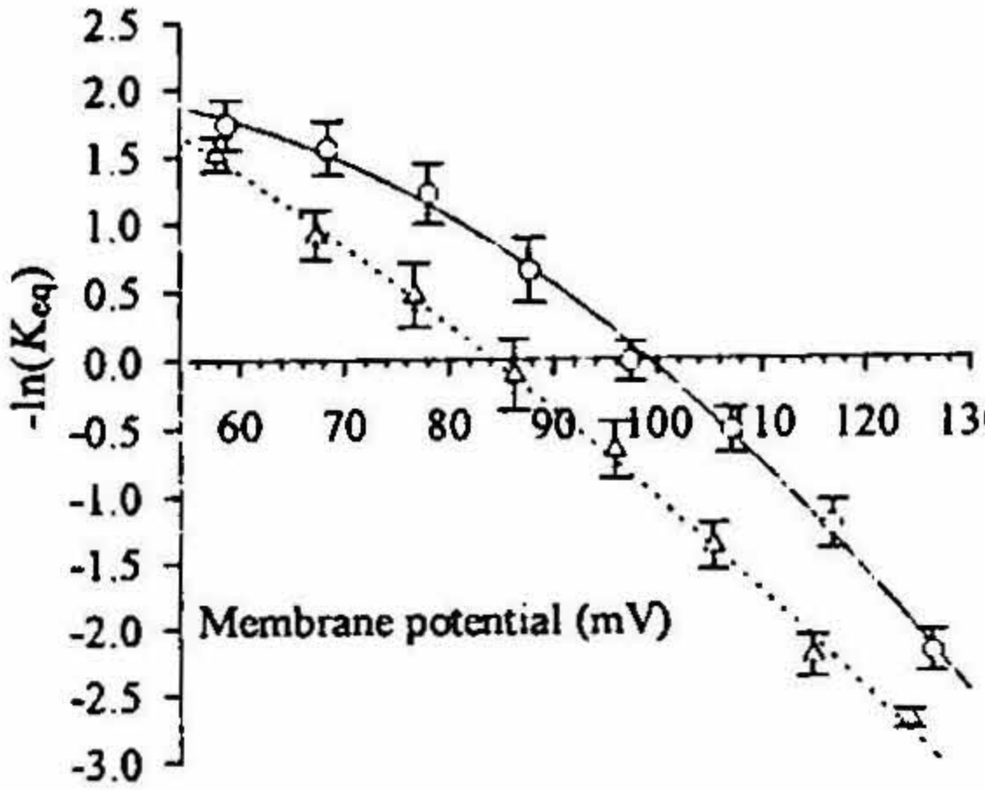

FIG. 3. Plot of $\ln(K_{eq})$ vs temperature and potential. Plot of $-\ln(K_{eq})$ vs membrane potential at two temperatures. $\ln(K_{eq})$ is zero at 99.8 and 86.0 mV at 15 (circle) and 35°C (triangle), respectively. The fit is with a quadratic regression.

for a voltage-gated ion channel free energy change with potential is linear.[7, 8] Recent studies have shown that voltage sensor interacts with other domains of channel.[9, 10] Thus, the movement of the voltage-sensing domain, during voltage gating, would influence other parts of the channel molecule and such changes should be reflected in the channel's voltage dependence. Taking into account the interaction energy, the relation between voltage and free energy change between open and close state will be given by:

$$Uy = U_0 + (cyV/d) + (1/2)a(y - y_0)^2 \qquad (3)$$

where U_0 is energy and y_0 the position of the charge c when the trans-membrane potential is zero, i.e. $V = 0$, d the thickness of the membrane and a the coefficient of rigidity (a type of spring constant) that affects the movement of charge containing domain.[6] At equilibrium, i.e. $(d(Uy)/dy = 0)$, solving and substituting the expression for y into eqn 3 gives:

$$Uy = U_0 + (cy_0V/d) - (1/2a)(cV/d)^2. \qquad (4)$$

Equation (4) shows that the change in free energy with membrane potential will be quadratic if the voltage sensor interacts with other domains of the channel. The reduction in curvature with increase in temperature can be explained by thermodynamics and kinetic energy of the channel molecule at various temperatures. At low temperature (15°C) the molecule will be rigid and thus any change in structure would require more input of energy, which would reduce at higher temperature (35°C). This also exemplifies the importance of the physiological temperature for the optimal efficiency of biological molecules.

The channel reported here has a temperature-sensitive, voltage-dependent rate-limiting step associated with channel opening, at low intracellular calcium. Our study shows physiological temperature for mammalian K^+ channels is important for channel function, because at these temperatures the channel overcomes the pull or restraint on the voltage sensor by other parts of channel with much lower input of energy in the form of voltage change. Thermodynamic studies together with electrophysiology are a potential area for a better understanding of channel structure and function.

Reference

1. HAMILL, O. P., MARTY, A., NEHER, E. AND SAKMANN, B. *Pflugers Archiv.*, 1981, **391**, 85.

2. HODGKIN, A. L. AND HUXLEY, A. F. *J. Physiol.*, 1952, **117**, 500.
3. RUDY, B. *Neuroscience*, 1988, **25**, 729.
4. PETERSEN, O. H. AND MARUYAMA, Y. *Nature*, 1984, **307**, 693.
5. MASON, W. T. AND WARING, D. W. *Neuroendocrinology*, 1986, **43**, 205.
6. HILL, T. L. AND CHEN, Y-D. *Proc. Natn Acad. Sci., USA*, 1972, **69**, 1723.
7. STEVENS, C. S. *Biophys. J.*, 1978, **22**, 295.
8. MOCZYDLOWSKI, E. *Ion-channel reconstitution* (C. Miller, ed.) Plenum Press, 1986, pp. 92–101.
9. MCCORMACK, K. *et al.* *Proc. Natn Acad. Sci., USA*, 1991, **88**, 2931.
10. TOMASELLI, G. F. *et al.* *Biophys. J.*, 1995, **68**, 1814.

Thesis Abstract (Ph. D.)

Stereochemical analysis on protein structures—Lessons for design, engineering and prediction by K. Gunasekaran
Research supervisor: Prof. C. Ramakrishnan
Department: Molecular Biophysics Unit

1. Introduction

Proteins are polypeptide chains made up of L-amino-acid residues linked together in a definite sequence. Christian Anfinsen, in 1960s, through his seminal work on ribonuclease demonstrated that the information necessary for a polypeptide chain to fold into a unique three-dimensional structure is encoded in the linear amino-acid sequence.[1] The advent of X-ray crystallographic methods in the determination of protein structure has resulted in vast accumulation of structural information, providing opportunity to study the different aspects of protein structure. For the past quarter century, conformational analysis in dihedral (ϕ, ψ) angle space has emerged as powerful tool for examining large structures where each individual residue can be structurally characterized by a single set of (ϕ, ψ) values.[2] The study presented in the work deals with the analysis of protein crystal structures with emphasis on backbone stereochemistry. The investigations involve identification and analysis of common structural features observed among the unrelated protein crystal structures which are available in the Brookhaven Protein Data Bank (PDB). The work, in essence, attempts to provide a rational knowledge base for design of protein structural mimics, protein engineering and structure prediction.

2. Materials and methods

A dataset of 250, largely nonhomologous, high-resolution (≤ 2.0 Å) protein structures from PDB has been selected for the purpose of studying various structural aspects. Figure 1 shows the scheme used in the selection procedure. Secondary structures were identified based on the backbone dihedral angle (ϕ, ψ) criteria [right-handed helical conformation–α_R: $\phi = -140°$ to $-30°$ and $\psi = -90°$ to 45°; left-handed helical conformation $-\alpha_L$: $\phi = 20°$ to 125° and $\psi = -45°$ to 90°; extended conformation $-E$: $\phi = -180°$ to $-30°$ and $\psi = 60°$ to 180° and $-180°$ to $-150°$). We now discuss the various structural aspects investigated.

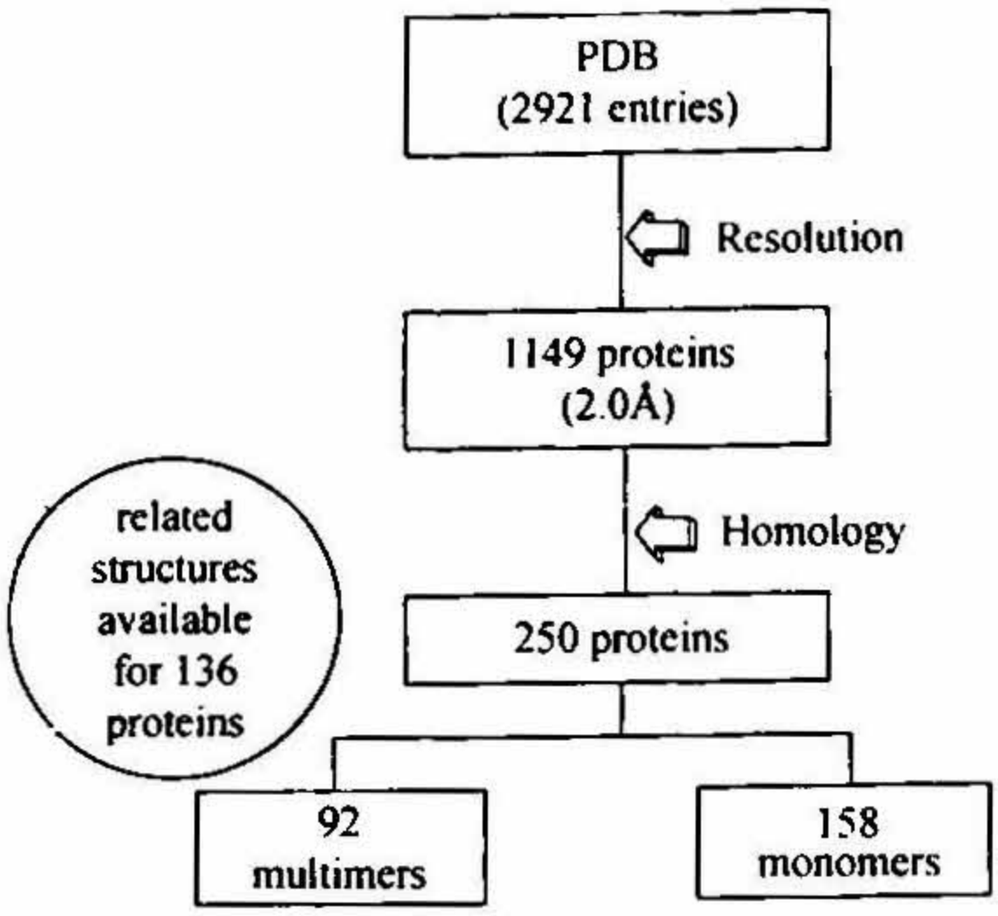

FIG. 1. Flowchart of the scheme used in the selection of 250 nonhomologous, high-resolution (≤ 2.0 Å) protein crystal structures (also referred to as representative dataset.)

3.1. *Ramachandran-disallowed conformations in protein structures*

A dataset consisting of 110 high-resolution, nonhomologous, protein crystal structures from PDB was examined (it may be noted that this particular analysis was carried out at the early stages with the available dataset then in the laboratory). Residues falling outside the defined 'broadly allowed limits' on the Ramachandran map were chosen and the reported B-factor value of the α-carbon atoms was used to further select the well-defined disallowed conformations. The conformations of the selected 66 disallowed residues clustered in distinct regions of the Ramachandran map indicating that specific ϕ, ψ distortions are preferred under compulsions imposed by local constraints. The distribution of various amino-acid residues in the disallowed residue dataset showed a predominance of small polar/charged residues with bulky hydrophobic residues being infrequent. An analysis on short contacts reveals that they are eliminated in most cases by local distortions of bond angles. The identified disallowed residues are mostly conserved related protein structures.

3.2. *Helix termination signals in protein structures*

A dataset of 1057 helices were identified from the 250 high-resolution (≤ 2.0 Å), nonhomologous, protein crystal structures. The backbone dihedral angles (ϕ, ψ) of the terminating residue (T) were found to cluster either in the left-handed helical region [469 helices (44%)] or in the extended region [459 helices (43%)] of the Ramachandran map. Gly residues were found to have an overwhelming preference to occur as the α_L-terminator (T) resulting in the classical Schellman motif, with a strong preference for hydrophobic residues at position $T-4$ and $T+1$. In the case of E-terminated helices, His, Asn, Leu and Phe were found to occur with high propensity at position T. Pro residues were absent at position T, but had the highest propensity at position $T+1$. An examination of the frequencies of hydrophobic (h) and polar (p) residues at position flanking Gly/Pro reveals that Pro residues flanked by polar amino acids have a very strong tendency to terminate helices. An examination of a segment ranging from $T-4$ to $T+3$ appeared to be necessary to determine whether helix termination or continuation occurs at Gly residues. The two types of helix termination (α_L, E) signals also differed dramatically in their solvent accessibility.

3.3. *β-Hairpins in proteins*

A total of 311 short-loop (≤ 5 residues) β-hairpins were identified from the dataset of 250 high-resolution (≤ 2.0 Å), nonhomologous protein crystal structures. Type-I′ and II′ β-turns were found to have a high propensity for occurrence in 2-residue loops. For 3- and 4-residue loops, the major conformational motif in the linking segments is α_R-α_R-α_L and α_R-α_R-α_R-α_L, respectively. The present larger dataset confirms the high occurrences of these motifs that have been identified in earlier analyses.[3,4] In addition to type-I′ and II′ β-turns, several examples of type-I β-turn nucleated 2-residue loop hairpins have also been observed in spite of having opposing sense of twist to that of type-I′ β-turn. The larger number of examples in this study allows estimation of the specific amino-acid preferences for loop positions in 2, 3 and 4 residue loops. Small polar residues Asn, Asp, Ser, Thr and Gly and Pro in general have a high propensity for the loop positions but they reveal specific positional preferences in these frequently occurring motifs. There are no strong compositional preferences in the strand segments. Several Cys–Cys pairs have been identified at the nonhydrogen-bonded positions of β-hairpins; as many as 6 are disulfide-bonded pairs.

3.4. *β-Turn interconversions in protein structures*

Of the 250 high-resolution (≤ 2.0 Å), nonhomologous protein crystal structures, 136 proteins had 'homologous entries' (alternate structures, complexes, site-specific mutants or homologous sequences from different sources) in the PDB which have sequence homology > 40% and the structure determined at high resolution (≤ 2 Å). Based on the sequence alignment of the representative protein with each of its 'homologous entries', 55 examples of β-turns undergoing conformational interconversions (Type I/III ⇝ Type II or Type I′/III/ ⇝ Type II′) were identified. An examination of the secondary structures at the flanking positions of the 55 examples of β-turns reveals that significant number of the examples (16) occur in short segments (≤ 6 residues) linking the secondary structures. A further examination reveals that 7 examples occur in the loop region of the β-hairpins indicating that the formation of ordered secondary structures on either side of the β-turn does not preclude local conformational dynamics. In β-turns undergoing flips, Pro (11 examples), Lys (9 examples) and Ser (7 examples) were most often found at the $i+1$ position. Glycine was found to occur overwhelmingly at the position $i+2$ (28 examples) while Ser (7 examples) and Asn (6 examples) were amongst the most frequent residues. In order to estimate the energy barrier for the type I ⇝ type II β-turn interconversions, peptide models Ac-Pro-Aib-NHMe and Ac-Pro-Gly-NHMe were chosen. The AM1 level calculation reveals that the path which corresponds to the outward rotation of the central carbonyl group is barrierless (3.2 kcal/mol in the case of Ac-Pro-Aib-NHMe and 2.8 kcal/mol in the case of Ac-Pro-Gly-NHMe) suggesting that concerted flips of central peptide units involving correlated single bond rotation can occur with *essentially* negligible activation energy barriers.

3.5. *Protein motifs: Analysis on V3 loop of HIV-1 gp120*

Residues adopting left-handed helical conformation (α_L) were identified from the dataset of 250 high-resolution (≤ 2.0 Å), nonhomologous high-resolution (≤ 2.0 Å) protein crystal structures. Of the 2574 residues found to adopt α_L conformation, 1510 correspond to Gly residues,

representing the majority of the examples and 1062 to nonGly residues. A novel multiple turn conformation, which involves α_L, has been observed for a segment GPGRAFY in the crystal structure of a complex of HIV-1 gp120 V3 loop peptide with the Fab fragment of a neutralizing antibody.[5] A structural motif has been defined for the peptide segment, employing idealized backbone conformations characterized by ranges of virtual C^α torsion and bond angles. A search of the 250 protein crystal structures permitted identification of 64 examples of similar structural motifs. Two major conformational families have been identified, which differ primarily in the conformation at residue 3. The observed conformation at residue 3 in family 1 is left-handed helical (α_L) and that in family 2 is right-handed helical (α_R). Of the 30 examples in family 1, 17 examples have Gly residues at position 3. Of the 31 examples in family 2, 10 have Asn/Asp at position 3. Computer modeling of the V3 loop tip sequence using the two backbone conformational families as starting points leads to minimum-energy conformations in which antigenically important side-chains occupy similar spatial arrangements.

3.6. *Structural analysis on membrane proteins–An introduction*

Our laboratory has recently been interested in studying membrane protein structures and their comparison with water-soluble globular proteins with the goal to predict the conformation of the membrane-spanning segments. A dataset consisting of 55 membrane protein sequences, for which experimental information was available, were obtained from the SWISS-PROT sequence database. Examination of the amino-acid preferences to occur in the transmembrane segments and in the interior of the water-soluble globular proteins reveals that both have similar characteristics in their nature of chemical polarity. An analysis on amino-acid positional preferences in globular and membrane protein helices has also been carried out.

The study presented in this work has implication in the design of structurally and functionally important motifs, protein engineering, and structure predictions.

References

1. ANFINSEN, C. B. *Science*, 1973, **181**, 223.
2. RAMACHANDRAN, G. N., RAMAKRISHNAN, C. AND SASISEKHARAN, V. *J. Mol. Biol.*, 1963, **7**, 95.
3. SIBANDA, B. L. AND THORNTON, J. M. *Nature*, 1985, **316**, 170.
4. SIBANDA, B. L., BLUNDELL, T. L. AND THORNTON, J. M. *J. Mol. Biol.*, 1989, **206**, 759.
5. GHIARA, J. B. *et al.* *Science*, 1994, **264**, 82.

Thesis Abstract (Ph.D.)

Hyperplane partitioning: An approach to global data partitioning for distributed memory machines by S. R. Prakash
Research supervisor: Prof. Y. N. Srikant
Department: Computer Science and Automation

1. Introduction

Data partitioning (or distribution) for distributed memory machines (DMMs) has been a difficult problem. Significant amount of work has been done in getting more parallelism from the programs.[1] However, without reducing communication overhead in the programs, they cannot be expected to run efficiently. There have been efforts in which the programmers are asked to give data allocation themselves and compiler will generate code automatically.[2] This might prove to be very difficult for programmers especially when the loops contain numerous array references. Reduction in communication overhead has been studied by many researchers. Ramanujam and Sadayappan[3] tried to transform the programs to get parallelism as well as reduce communication overhead. It has been seen[4] that for a loop whose access patterns cannot be statically analyzed to get the best partitioning, compilers have traditionally generated sequential code. Although this pessimistic strategy is safe and simple, it essentially precludes the automatic parallelization of entire class of programs with irregular domains and/or dynamically changing interactions. For such loops, the general strategy adopted is to use *inspector*, *scheduler* and *executer* codes.[4] However, such techniques are for shared memory machines, where there is no problem of data partitioning.

In this paper, we propose a method by which we can find a partition of a nested do-loops which reduces communication when executed on distributed memory machines. Our method differs from the other works in the following ways: *firstly*, no assumptions are made regarding whether loops are do all or not, as assumed in Agarwal *et al.*[5] *Secondly*, the array references that are in the loops can have any linear functions of induction variables, not just $\vec{i} + \vec{c}$ type of functions of loop indices as assumed in Banerjee[1] and others, where $\vec{i}$ is index vector and $\vec{c}$ a constant vector. Such functions of loop indices can lead to non-uniform dependences. According to an empirical study, 44.34% of the two-dimensional array references contain coupled-subscripts,[6] and most compilers run them sequentially due to difficulty in analyzing such loops.

2. Hyperplane partitioning

We first see the program model assumed in this work and later will see how to partition the iteration space using *hyperplane partitioning*.

2.1. *Program model*

In general, scientific programs contain a large number of array references in nested loops. In such programs, nested loops are main source of parallelism and are most time-consuming parts. A normalized n-nested loop[1] is considered in this work.

The body of the loop, $H[i_1, i_2, \ldots, i_n]$, contains a set of assignment statements possibly containing array references. The array references considered in this work are of the form, $X(a_{11}i_1 + a_{12}i_2 + \ldots + a_{1n}i_n + a_{01}, \ldots\ldots, a_{m1}i_1 + \ldots + a_{mn}i_n + a_{0n})$, which can be compactly written as $X\left(A\vec{i} + \vec{a}_0\right)$ where

$$A = \begin{bmatrix} a_{11} & a_{12} & \cdots & a_{1n} \\ a_{21} & a_{22} & \cdots & a_{2n} \\ \cdots & & & \\ a_{m1} & a_{m2} & \cdots & a_{mn} \end{bmatrix}, \vec{a}_0^T = \begin{pmatrix} a_{01} & a_{02} & \cdots & a_{0m} \end{pmatrix}$$

In this work, without any loss of generality, we assume that $m = n$. This assumption will not reduce the generality as we can add dummy dimensions, if $m < n$, or we can add dummy loops which run for 0 times if $n < m$.

2.2. *Iteration space partitioning*

Consider the following example.

Example 1

```
for i = 0 to N/2 do
   for j = 0 to N/2 do
      begin
         A[i + 2j, i+ j] = A[i, j] + B[i, j]
         B[i, j] = A[i, j] *2
      end;
```

The dependence graph for Example 1, given in Fig. 1(a) shows how the index points are dependent on each other.

The problem here is to find the iteration partition such that the communication that is incurred in executing these partitions will be as less as possible. Finding the best possible partition, which is zero-communication partition, will require, finding the *vertical partition* of the dependence graph[1] which, in general, requires spanning the entire iteration space. This will take enormous amount of time especially when the number of loops is many and each running over a large number of iterations.

2.3. *Computing the hyperplane of partition*

The method to compute the hyperplane of partition, in brief, is as follows.

- First, for every pair of references, the dependence equation is computed.
- For each pair, the direction of dependence is computed.
- From these directions of dependences, we compute a hyperplane which is used to partition the iteration space into as many number of partitions as there are logical processors.

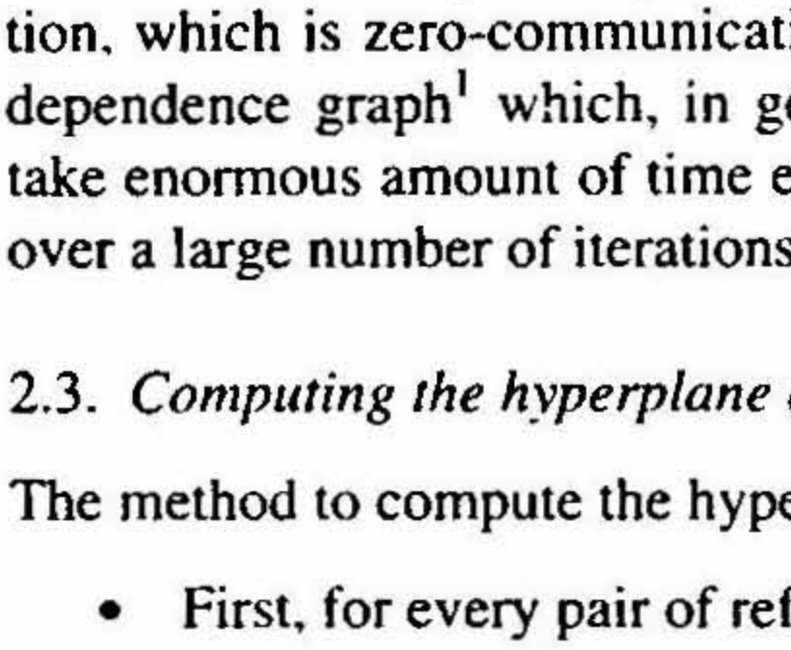

(a) Dependence graph

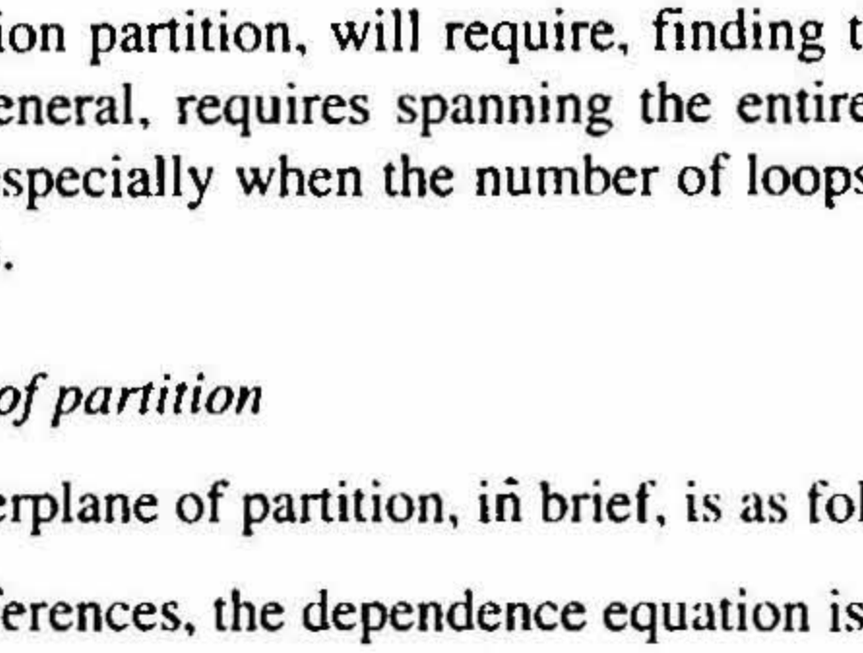

(b) The Nature of dependences

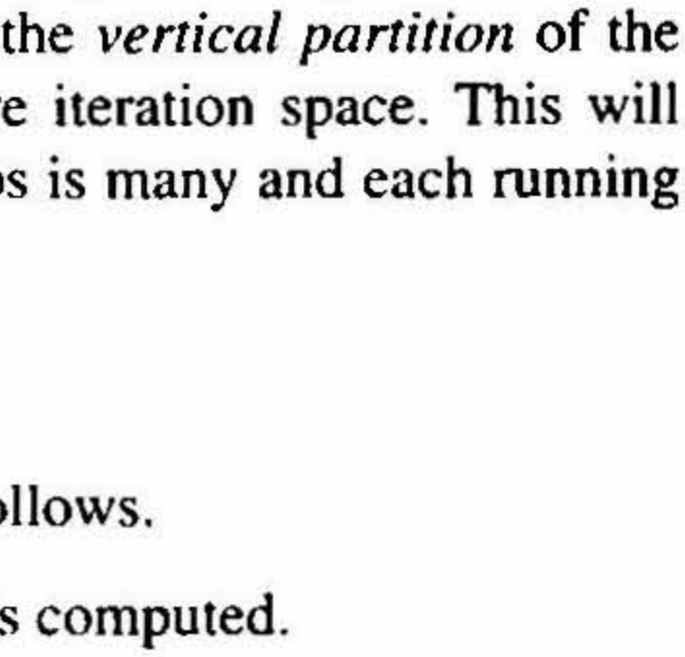

(c) Best fit line for given lines

FIG. 1(a) Dependence graph, (b) Nature of dependences, and (c) Best-fit line.

- These dependence directions induce data space partitions in every array used in the loop.
- Each logical processor executes different partition in parallel keeping corresponding data partitions locally, and synchronization and nonlocal accesses are handled at run-time.

Consider a loop given in Example 1. There are two arrays that are accessed in the loop. We see that the need for communication arises only when there is dependence between iterations. On such situations, different processors try to access the same data which is owned by only one of them. If we localize such dependences (i.e. run both the source and target iterations on the same processor) and keep the data accessed by the iteration locally then we have removed the necessity to communicate nonlocal data to both synchronizations between processors (to satisfy inter-iteration dependences), thus reducing the overall communication. For Example 1, the dependence graph for $N = 16$ is shown in Fig. 1(a). As can be seen, the dependence directions tend to align themselves along a particular direction (in this case the direction of (–0.67,1)), provided the conditions (given later) hold. By partitioning the iteration space along that direction and by placing the data accessed by these iterations locally, we can expect the communication to be reduced significantly. Further, since the dependence direction tends to align along a particular direction eventually, we expect the communication cost to reduce as the size of iteration space increases. In Fig. 1(b) we see the effect for Example 1 (the curve termed 'bm4.c'). Note also the same phenomenon does not happen with some standard HPF partitions like block distributions. Again referring to Fig. 1(b) the curve termed 'bm4.sc' shows this effect. The direction of convergence can be computed analytically for every pair of references in a loop and the hyperplane which 'best fits' these set of directions will be taken as the hyperplane of partition for the iteration space. This hyperplane is induced into different data spaces that are referenced in the loop to get the data partitions.

Theorem 2.1 (Dependence equation)

The general dependence equation for the array references, $X[A\vec{i} + a_0]$ *and* $X[B\vec{i} + b_0]$ *is given by:* $\vec{d} = C\vec{i} + c_0$, *where* $C = B^{-1}(A - B)$, $c_0 = B^{-1}(a_0 - b_0)$ *and any* $\vec{j} \succ \vec{i}$ *depends on* $\vec{i}$ *if* $\vec{j} = \vec{i} + \vec{d}$. (See Prakash[7] for proof).

In the above theorem, it is assumed that the coefficient matrices are nonsingular, i.e. inverses exist. The case of singular matrices is dealt with in Prakash.[7]

Definition 2.1 (Trajectory of index points): For a given pair of references, for a given loop with lower bounds $l\vec{b}$ and upper bounds $u\vec{b}$, we can build a trajectory of index points by applying repeatedly the dependence equation from an initial index point $\vec{s}$ which takes us to the final index point $\vec{f}$, where both $\vec{s}$ and $\vec{f}$ lie between $l\vec{b}$ and $u\vec{b}$.

Definition 2.2 (Direction of dependence): The direction of dependence for a pair of reference, having subscript functions, $A\vec{i} + a_0$ and $B\vec{i} + b_0$, is defined as the direction $\vec{d}_k$ such that $\vec{d}_{k+1} = \eta\vec{d}_k$, where $\vec{d}_{k+1}$ and $\vec{d}_k$ are dependence directions at two adjacent points on the trajec-

tory of index points for the given pair of references and η is constant, provided such a constant exists. Otherwise direction of dependence is said to be oscillatory.

Theorem 2.2 (Direction of dependence)

Suppose $D = C + I$ (where C is the matrix of the dependence equation). The direction of dependence for a pair of references, having subscript functions, $A\vec{i} + a_0$ and $B\vec{i} + b_0$, is the eigenvector of the matrix, D, corresponding to the dominant eigenvalue of that matrix, if D has n linearly independent eigenvectors and D a dominant eigenvalue. (See Prakash[7] for proof.)

Theorem 2.2 also says that this need not happen always, the other case being when such eigenvalue does not exist. Then, the trajectory either will revolve round the origin spirally or diverge depending on whether the eigenvalues are not real or real, respectively. For such cases refer to Prakash.[7] In this section, we will see how to get the hyperplane which partitions the iteration space into as many tiles as the number of processors. These tiles can be used to induce data partition in the data space using a particular reference in the loop for every array in the loop. These tiles and the corresponding data partitions can be placed in the local memory of the respective processor, and we can run those partitions in parallel by introducing the synchronizing messages to handle dependences. The hyperplane that minimizes the deviations from the given directions will be the one which minimizes the sum-squared of the sine of the angle between the hyperplane and the directions (Fig. 1(c)). See Prakash[7] for details.

Theorem 2.3 (The best fit hyperplane)

Given p lines in n dimensions, with direction cosines, Δx_{ij}, $1 \le i \le p$, $1 \le j \le n$, passing through the origin, the hyperplane, $\sum_{j=1}^{n} a_j x_j = 0$ which also passes through the origin and is the best fit for the points at unit distance from the origin has the coefficients a_j, $1 \le j \le n$, such that $Xa = b$, where the matrix $X_{kj} = \sum_{i=1}^{p} \Delta x_{ik} \Delta x_{ij}$, for $n - 1 \ge j, k \ge 1$ and $b_k = -\sum_{i=1}^{p} \Delta x_{ik} \Delta x_{in}$, for $n - 1 \ge k \ge 1$ and $a_n = 1$. (See Prakash[7] for proof.).

Finally, we need to partition the array data space from the iteration partition. The hyperplane that we got from the above analysis can be induced into the array data spaces also.

3. Global data partitioning

The hyperplane partitioning technique explained above is for local optimization, i.e. for a loop. The same technique can be applied to a sequence of loops which ensures minimal communication for all the loops taken together when run on a DMM. This needs a good communication cost estimator, which estimates the communication that would be incurred if the given loop is run with given iteration and data partitions.[8] The details of global data partitioning can be seen in Prakash and Srikant.[8] The tool, *hyperplane partitioner*, which we have developed will do the *global data partitioning*. It also does some compiler optimizations like space, time and message optimizations.[9]

The hyperplane partitioner was tested for performance on some benchmark programs from NAS and some programs designed by us to show the merits of the tool. The benchmarks se-

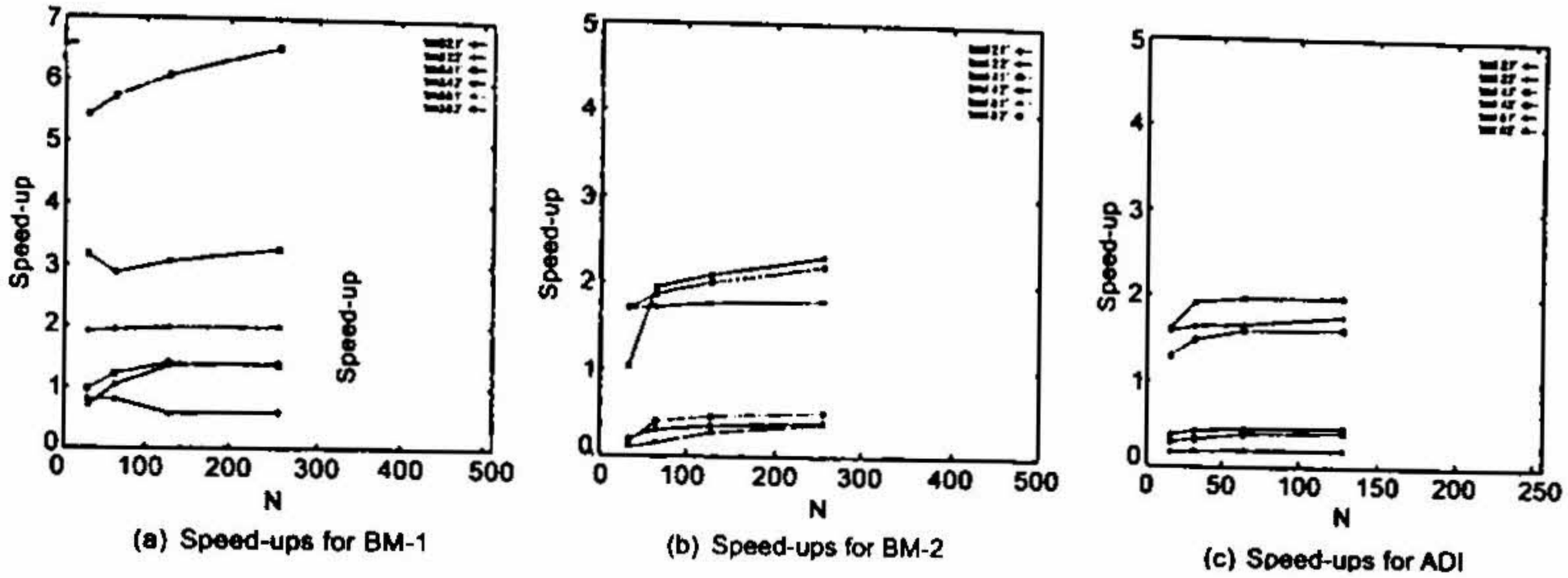

(a) Speed-ups for BM-1 (b) Speed-ups for BM-2 (c) Speed-ups for ADI

FIG. 2. The speed-ups for different benchmarks.

lected were ADI (alternating direction implicit) and SYR2K. We give the results for ADI here. (Refer Prakash[7] for SYR2K results).

ADI program has 6 loops with both single- and two-nested loops. Since the ADI loops are very short, we unroll the loops a few times, and then run them in parallel. The global data partitioner had found that the best way to run the program is by partitioning the loop sequence into two regions, first with first three loops, and the second with the last three loops; notationally it is {{123},{456}}. The partition plane for the first set had the coefficients (1, 0) and for the second set (0, 1), which is (BLOCK,*) and (*,BLOCK) partitions, respectively. Figure 2(c) shows the speed-ups for this benchmark for different sizes of arrays and different number of processors. In the figure, 'bmx.n.y' gives the performance for benchmark BM-x for 'n' processors. The number of times the loops were unrolled is given by 'y', which varies from benchmark to benchmark and is found experimentally. In this case, if 'y' is 1 means we have to unroll 100 times and if 2 it is 1000 times.

The first of our programs (BM-1) has five loops with three two-dimensional arrays. All the loops access the arrays in a similar manner (has the same dependence direction). This program is to show that the tool finds the static distribution if those are the best. Figure 2(a) shows the performance on IBM-SP2 for different sizes of arrays and different number of processors. For IBM-SP2, it has chosen to run all the loops with the same partition of the data spaces, i.e, {{0-4}} with the same hyperplane with coefficients (1, −1). The second program (BM-2) has six loops with no static partition. There are three arrays accessed in different ways in different loops. For IBM-SP2, it decides to partition the loops as {{01}{2}{345}}. Figure 2(b) shows the performance on IBM-SP2 for {{01}{2}{345}}. We also saw by experiments that speed-ups for these programs with both BLOCK and CYCLIC distributions are inferior compared to partitions which our tool has suggested. See Prakash[7] for more details.

5. Conclusions

We have seen that there are many cases where we encounter loops which have coupled sub-scripts and we want to effectively run them on DMMs. The implementation results show good performance for our tool with such non-uniform dependences. The tool also finds HPF-like distributions whenever such distributions are good. Inter-procedural data partitioning analysis

and a good scheme for global data partitioning for a general program are lacking in the current implementation.

References

1. BANERJEE, U. *Loop transformations for restructuring compilers: The foundations*, Kluwer Academic, 1993.
2. KOELBEL, C. H. AND MEHROTRA, P. Compiling global name-space parallel loops for distributed execution. *IEEE Trans.*, 1991, **PDS-2**, 440–451.
3. RAMANUJAM, J. AND SADAYAPPAN, P. Compile-time techniques for data distribution in distributed memory machines. *IEEE Trans.*, 1991, **PDS-2**, 472–482.
4. RAUCHWERGER, L., AMATO, N. M. AND PADUA, D. A. A scalable method for run-time loop parallelization, *Int. J. Parallel Programming*, 1995, **23**, 537–576.
5. AGARWAL, A., KRANZ, D. AND NATARAJAN, V. Automatic partitioning of parallel loops and data distribution for distributed shared-memory multiprocessors, *IEEE Trans.*, 1995, **PDS-6**, 943–962.
6. SHEN, Z., LI, Z. AND YEW, P. C. An empirical study of array subscripts and data dependencies, *1989 Int. Conf. on Parallel Processing*, Vol. II, pp. 145–152, St. Charles, Ill., Aug. 1989.
7. PRAKASH, S. R. *Hyperplane partitioning: An approach to global data partitioning for distributed memory machines*, Ph.D. dissertation, Indian Institute of Science, Bangalore, July 1998.
8. PRAKASH, S. R. AND SRIKANT, Y. N. Communication cost estimation and global data distribution for distributed memory machines, *Int. Conf. on High Performance Computing*, Bangalore, India, Dec. 1997.
9. PRAKASH, S. R. AND SRIKANT, Y. N. Hyperplane partitioninig: An approach to global data partitioning for distributed memory machines, *13th Int. Parallel Processing Symp.*, San Juan, Peurto Rico, April 1999.

Thesis Abstract (Ph.D.)

The effect of pH and surface potential on the ligand binding properties, stability and unfolding pathway of abrin-II, a ribosome-inactivating protein by J. Krupakar

Research supervisor: Prof. P. K. Das
Department: Inorganic and Physical Chemistry

1. Introduction

Abrin-II, a heterodimeric, ribosome-inactivating protein (RIP) toxin from *Abrus precatorius* seeds, consists of two polypeptide subunits, viz. A-(M_r 30,000) and B-(M_r 33,000). The two are connected through a single disulfide bond.[1, 2] The A-subunit is an N-glycosidase, and inactivates eucaryotic protein synthesis by cleaving the adenine 4324 residue from the 28S rRNA.[3] The B-subunit is a lectin, binds to the cell-surface receptor that contains terminal galactose and facilitates the entry of the toxin to the cytosol. RIPs have been used for the preparation of immunotoxins with potential uses in therapy against cancer and infectious diseases including AIDS.[4] Since their targets are in cytosol, they reach their targets by translocating across a

membrane bilayer. By virtue of their ability to translocate across the membranes, these toxins are viewed as valuable tools in understanding the nature of protein–membrane interaction and transmembrane translocation of cellular proteins. They also agglutinate cells. However, the effect of surface potential (membrane potential) on agglutination of cells by abrus precatorius agglutinin-II (APA-II, noncovalent dimmer of A-s-s-B) and abrin-II has not yet been elucidated.

The toxin passes through a minimum of five steps for the manifestation of its biological activity: (a) binding to cell surface via the B-subunit, (b) internalization, (c) reduction of the inter-subunit disulfide bond, (d) transmembrane transport of the A-subunit to the cytosol, and (e) inhibition of protein synthesis by the catalytic action of the A-subunit. It is well known that the toxin binds to cell surface receptors[5] and enters the cell via receptor-mediated endocytosis.[6] It is also established that the reduction of disulfide bond is necessary for the action of toxin.[7] Earlier it was thought that the late endosomes[8] and Golgi[9] were probable sites for transmembrane transfer of a toxin. Recently it has been suggested that the endoplasmic reticulum is a probable site[10] for the transfer. However, the mechanism underlying the transmembrane transport by RIPs is not clearly understood.

2. Experimental

In this study, surface potential of model membrane containing varying mole per cents of (a) monosialoganglioside, G_{M1} and phosphatidylcholine, DPPC, (b) DPPC and phosphatidic acid, DMPA, (c) asialomonosialoganglioside, aG_{M1}, G_{M1} and DPPC and (d) aG_{M1}, DMPA and DPPC has been measured by using the principle of partitioning of metachromatic dyes acridine organe, AO and methylene blue, MB between the membrane and bulk phases.[11] Membrane potential increases with increase in the mole per cent of the negatively charged lipid in the membrane. Both APA-II and abrin-II are able to aggregate model membranes containing neutral gangliosides, aG_{M1}. The aggregation has been monitored by time-dependent increase in scattering intensity at 400 nm. The addition of negatively charged lipids decreases the extent of aggregation by APA-II and abrin-II. These results indicate that the surface potential influences the aggregation of membranes containing aG_{M1} by APA-II and abrin-II. That aggregated complex is dissociated by lactose suggests that aggregation is mediated by glycolipid–protein interaction.

The effect of pH on ligand properties, conformation, stability and unfolding pathway of abrin-II was investigated by means of fluorescence, far- and near-UV-circular dichroism (CD) and calorimetric measurements. The intrinsic fluorescence of abrin-II does not change with the addition of lactose or galactose. Therefore, initially the binding constant and the number of binding sites for lactose to abrin-II were measured by isothermal titration calorimetry (ITC). ITC needs a large quantity of protein particularly for low-binding constants while fluorescence-based methods need only a small quantity of protein. Therefore, fluorescently labelled galactose was used to study sugar-binding properties of this toxin. Two binding sites with a binding constant of 2.98×10^3 M^{-1} at 9°C were obtained for lactose with abrin-II at pH 7.2 by ITC. The fluorescence-quenching data showed that at pH 7.2 and pH 4.5, the binding constants of methylumbelliferyl α-D-galactopyranoside to abrin-II at 25°C were 7.87×10^4 M^{-1} and 2.52×10^4 M^{-1} and the number of binding sites was 1.65 and 1.33, respectively. The low-

binding constant and the small number of binding sites at pH 4.5 than at pH 7.2 indicate that most of the abrin-II molecules are dissociated from their receptors in the endosomes. Environment-sensitive hydrophobic probes like bis-ANS, (4, 4′-dianilino-1, 1′-binaphtyl-5, 5′-disulfonic acid) and ANS (8, 1-anilino naphthalene sulfonic acid) have been employed to monitor changes in the conformation of abrin-II and its A-subunit at pH 7.2 and pH 4.5. At pH 4.5, abrin-II and the A-subunit expose more hydrophobic patches to the surface than at pH 7.2. The A-subunit is more hydrophobic than the intact abrin-II at both pH 7.2 or pH 4.5. These results suggest that abrin-II and the A-subunit undergo subtle changes in their conformation at both these pH values. Intrinsic protein fluorescence, far- and near-UV-CD spectroscopy and ANS binding in the presence of varying amount of guanidine hydrochloride studies reveal that the unfolding of abrin-II occurs through two intermediates at pH 7.2 and one intermediate at pH 4.5.[12] At pH 7.2, the two subunits A and B of abrin-II unfold sequentially. The native protein is more stable at pH 4.5 than at pH 7.2. However, the stability of the abrin-II A-subunit is not affected by any change in the pH. Differential scanning calorimetric scan consists of two peaks corresponding to the A and B-subunits as confirmed by transition temperature and calorimetric enthalpy of the isolated abrin-II A-subunit. Abrin-II displays increased stability as the pH is decreased from 10.16 to 4.5. Lactose stabilizes the native conformation of abrin-II. This effect is more pronounced at pH 7.2. Analysis of the data obtained by differential scanning calorimetry in the presence of lactose suggests that two lactose molecules bind to one molecule of abrin-II. Changes in excess heat capacities 26.82 kJ mol^{-1} K^{-1} for the B-subunit and 19.71 kJ mol^{-1} K^{-1} for the A-subunit in the intact abrin-II are obtained.[13]

From the transmembrane translocation point of view, abrin-II enters into the cell through receptor-mediated endocytosis. At low pH in the endosomes, changes occur in the conformation of the toxin. These changes would allow the dissociation of a significant proportion of the toxin from its receptor, thus facilitating the recycling of the latter to the cell surface. The higher stability of the free toxin in the lumen of endosome not only would enable it to resist degradation but would also permit it to make its way to the Golgi apparatus and endoplasmic reticulum (ER). On reaching ER, the high pH of the compartment destabilizes the toxin thus permitting the reduction of inter-submit disulfide bond most likely by protein disulfide isomerase.[14] The released free A-submit from the intact abrin-II exposes more hydrophobic clusters and hence the A-subunit probably binds to the ER membranes. Then the A-subunit translocates into the cytosol.

References

1. Barbieri, L., Battelli, M. G. and Sterpi, S. — *Biochem. Biophys. Acta*, 1993, **1154**, 237–282.
2. Olsnes, S. and Phil, A. — In *Molecular action of toxins and viruses* (Cohen, P. and van Heyningen, S., eds), Elsevier, 1982, pp. 51–106.
3. Endo, Y., Tsurugi, K. and Lambert, J. M. — *Biochem. Biophys. Res. Commun.*, 1988, **150**, 1032–1036.
4. Thrush, G. R., Lark, L. R., Clinchy, B. C. and Vitetta, E. S. — *Rev. Immunol.*, 1996, **14**, 49–71.
5. Sandvig, K., Olsnes, S. and Phil, A. — *J. Biol. Chem.*, 1976, **251**, 3977–3984.
6. Refsnes, K., Olsnes, S. and Phil, A. — *J. Biol. Chem.*, 1974, **249**, 3557–3562.

7. MONTESANO, D., CAWLEY, D. AND HERSCHMAN, H. R. *Biochem. Biophys. Res. Commun.*, 1982, **109**, 7–13.

8. BEAUMELLE, B., ALAMI, M. AND HOPKINS, C. R. *J. Biol. Chem.*, 1993, **268**, 23661–23669.

9. YOSHIDA, T., CHEN, C., ZHANG, M. AND WU, H. C. *Expl Cell Res.*, 1991, **192**, 389–395.

10. RAPAK, A., FALNES, P. O. AND OLSNES, S. *Proc. Natn. Acad. Sci. USA*, 1997, **94**, 3783–3788.

11. NAKAGAKI, M., KATOH, I. AND HANDA, T. *Biochemistry*, 1981, **20**, 2208–2212.

12. KRUPAKAR, J., DAS, P. K. AND PODDER, S. K. *Biochem. Mol. Biol. Int.*, 1998, **46**, 415–424.

13. KRUPAKAR, J., SWAMINATHAN, C. P., DAS, P. K., SUROLIA, A. AND PODDER, S. K. *Biochem. J.*, 1999, **338**, 273–279.

14. ROBERTS, L. M. AND MICHAEL LORD, J. *J. Cell Biol.*, 1998, **140**, 733–736.

Thesis Abstract (Ph.D.)

Algorithms for routing, wavelength assignment and topology design in optical networks

by M. K. Rajesh
Research supervisor: Prof. Kumar N. Sivarajan
Department: Electrical Communication Engineering

1. Introduction

We consider optical networks implemented using wavelength division multiplexing (WDM) techniques. These networks are called wavelength-routed optical networks (WRONs). WDM is essentially frequency division multiplexing in the optical frequency domain. A *lightpath* is an end-to-end optical channel which is set up in a WRON by suitable optical switching and routing. These lightpaths could serve as high bandwidth pipes in a circuit-switched environment or could serve as the logical communication links (logical connections) for a variety of high-speed packet-switched networks.

We study three problems that arise in a WRON. The first problem is the design of optimal topologies for a packet-switched WRON.[1–3] The second is the problem of routing and wavelength assignment for lightpaths in a circuit-switched WRON.[4, 5] Finally, we consider the problem of designing the physical fiber topology of a WRON.[6]

The topology design of packet-switched WRONs involves (a) identifying the logical connections that are to be established, (b) setting up lightpaths (involves routing and wavelength assignment with no wavelength changers allowed) in the WRON to realize the logical connections, and (c) routing the traffic on the logical connections so as to satisfy the traffic demands. We present for the first time a linear formulation (integer linear program) for the topology design problem with the objective of minimizing the maximum offered load (congestion). The linear formulation takes into account the constraints which are imposed by the resources of the network and the design policies. The network resources are the number of wavelengths the fiber supports, the number of transmitters and receivers and the physical layout (number of fibers between the nodes). The design policies we consider are: (a) whether to allow multiple

connections between a source–destination pair or not, (b) to have full duplex or simplex logical connections, and (c) whether to limit the maximum number of hops a lightpath is allowed to take. We show by examples how the above constraints affect congestion. We prove that the optimum value obtained is the same if some of the inequality constraints in the linear formulation are replaced by equality constraints. This helps in reducing the search space of the integer linear program. For large networks we solve the linear program obtained by relaxing the integer constraints (LP-relaxation) by adding inequalities (cutting planes) which are valid for the LP-relaxation but are superfluous in the integer linear program. This LP-relaxation yields a lower bound on the congestion. One of the coefficients in the cutting planes we add is a lower bound on the congestion.[7] This enables us to iteratively improve the lower bound obtained by the LP-relaxation by using the previous value in each step as the lower bound in the next step. This not only helps in obtaining good lower bound but also forces some of the 0–1 variables close to zero or one which helps in rounding (setting variables to zero or one) the variables, to obtain a feasible solution to the integer linear program. We solved the LP-relaxation iteratively for a 14-node network (NSFNET) for various cases. The solutions obtained were then rounded to obtain logical connections and a routing and wavelength assignment for the logical connections. Subsequently, a linear program was solved to obtain a routing pattern for the packet-switched traffic on the logical connections. We note that in several cases the congestion obtained by rounding was very close to the lower bound on congestion obtained by solving the LP-relaxation.

In the problem of routing and wavelength assignment (RWA) in a circuit-switched WRON we consider two related problems. The first is that of maximizing the number of connections (*Max-RWA*) when the number wavelengths is fixed. The second problem is that of minimizing the number of wavelengths when the connections to be routed are fixed (*Min-RWA*). We show some new bounds that may be obtained for the *Max-RWA* and the *Min-RWA* problems. We present for the first time linear formulations (integer linear programs) for the *Max-RWA* and the *Min-RWA* problems which when solved provide the optimum solution when no wavelength changers are allowed (the case with full wavelength changers is easy to formulate). We solve the above linear formulation for small networks. For large networks we solve the LP-relaxation and then round the solutions to obtain a feasible solution for the integer linear formulation. We develop rounding algorithms and solve the *Max-RWA* and the *Min-RWA* problems for various networks (NSFNET, EONNET, UKNET).

Another interesting aspect we look at is how to obtain a linear formulation when we incorporate limited wavelength converters in a WRON. We, for the first time, give a linear formulation and prove that the inequalities of the formulation capture all valid routing and wavelength assignment possibilities in the WRON. We prove that if we impose some restrictions on the limited wavelength conversion capability then the number of constraints we need to consider is only quadratic in the number of wavelengths (in general, it is exponential in the number of wavelengths).

In the physical fiber topology design for WRONs, we consider the problem of minimizing the total working fiber length. In this problem we are given the connections to be set up, the physical layout, the unit cost of a link, and the maximum number of wavelengths supported by the fiber. Our objectives is to design a network capable of supporting all the connections with

minimum fiber length (proportional to cost). We, for the first time, present a linear formulation for the fiber topology problem, which, when, solved gives the optimum solution. As done earlier for large networks we develop rounding algorithms on the solutions obtained by solving the LP-relaxation to come up with a feasible solution to the integer-linear program. We show, and also illustrate with examples, that the bound on the cost obtained by solving a relaxed linear formulation approaches the optimum cost as the number of connectsion that have to be routed becomes large.

References

1. RAMASWAMI, R. AND SIVARAJAN, K. N. — Design of logical topoloties for wavelength-routed optical networks, *IEEE J.*, 1996, SAC-40, 840–851.
2. MUKHERJEE, B., BANERJEE, D. RAMAMURTHY, S. AND MUKHERJEE, A. — Some principles for designing a wide area optical network, *IEEE/ACM Trans. Networking*, 1996, 4, 684–696.
3. BANERJEE, D. AND MUKHERJEE, B. — Wavelength-routed optical network: Linear formulation, resource budgeting tradeoffs, and a reconfiguration study, *Proc. Infocom 1977.*
4. RAMASWAMI, R. AND SIVARAJAN, K. N. — Routing and wavelength assignment in all-optical networks, *IEEE/ACM Trans. Networking*, 1995, 3, 489–500.
5. BANERJEE, D. AND MUKHERJEE, B. — Practical approaches for routing and wavelength assignment in large all-optical wavelength-routed networks, *IEEE J.*, 1996, SAC-14, 1207–1217.
6. ALANYALI, M. AND AYANOGLU, E. — Provisioning algorithms for WDM optical network, *Proc. Infocom 1988.*
7. BIENSTOCK, D. AND GUNLUK, O. — Computational experience with a difficult mixed-integer multicommodity flow problem, *Math. Progm.*, 1995, 68, 213–237.

Thesis Abstract (M.Sc. (Engng))

Beneficiation studies on molybdenite ore from Harur area, Tamil Nadu by Indira Ravindran

Research supervisors: Prof. S. Subramanian and Dr M. S. Riyaz Ulla (Indian Bureau of Mines)
Department: Metallugry

1. Introduction

Molybdenum is a very important additive metal, used in the manufacture of steels, iron castings and alloys. Additionally, it is a refractory metal and has gained prominence as one of the nuclear and space-age metals.

Molybdenum does not occur in nature in its free or native state, but is only found chemically combined with other elements. Small deposits of molybdenum-bearing minerals occur throughout the world, but the only molybdenum mineral of commercial importance is molybdenite.

Primary molybdenite deposits are found in the United States, which has reserves accounting for 45% of the total world reserve base and the production is 40% of the total world output.[1] In India, almost all molybdenite is obtained currently as byproducts from copper and ura-

nium deposits. The present Indian production is only 66 tonnes while the demand is over 1000 tonnes. It thus becomes important to explore newer deposits of molybdenum and develop efficient beneficiation strategies to recover the metal. A potential source of primary molybdenite has been found in the Harur area of Dharmapuri district in Tamil Nadu.

2. Geology of Harur

Molybdenum mineralisation occurs in the shear zone. The shear zone contains quartz veins and chloritised/sericitised/altered epitode-hornblende gnesis carrying fine dusty/flaky molybdenite (fair to rich), galena, pyrite and chalcopyrite. It is reported that detailed exploration work by drilling up to the fourth level has been completed. The resource potential in the first two levels is of the order of 1.6 million tonnes with 0.018% Mo. The third- and fourth-level drilling has proved the persistence of mineralisation and the reserves are in the order of 2.6 million tonnes up to 300 m depth.[2]

3. Experimental materials and methods

Beneficiation studies have been undertaken on core-drill molybdenite ore samples from Vallampatti South block, Harur area, Tamil Nadu. The sample was crushed in jaw crusher to half inch size and further reduced in size in roll crusher to −10 mesh size. The product was screened in a 10- mesh vibrating screen. The experiments were carried out on −10 mesh sample. Reagents used are kerosene (collector for molybdenite), sodium dichromate and dextrin as depressants for galena and sodium cyanide as a depressant for copper mineral.

4. Results and discussion

4.1. *Characterisation of molybdenite ore sample*

Detailed characterization of the molybdenite ore has been carried out with respect to its mineralogy and chemical constituents. The studies indicate that quartz and sericite are the major minerals followed by carbonates and feldspar. Among the sulphide minerals, pyrite is dominant with trace amounts of galena, sphalerite, chalcopyrite and molybdenite. Molybdenite mostly occurred as medium-sized elongated plates and fine crystal aggregates in silicate matrix. Occasionally, flakes of molybdenite were found associated with pyrite and chalcopyrite, though molybdenite was not noticed in association with other sulphide minerals. At places, molybdenite was found as fine inclusions in silicates. The molybdenum content in the core sample is 0.1%, lead content is 0.06% and copper is 0.005%.

4.2. *Flotation studies*

The result of the flotation kinetic tests have shown that the percentage recovery and grade of molybdenum follow an inverse relationship with time. Studies carried out to evaluate different reagent combinations reveal that optimum values of grade and recovery could be achieved using kerosene and methyl iso-butyl carbinol (MIBC). Further, these studies have shown that a flotation time of 4 minutes is adequate, as the grade of molybdenum is found to deteriorate beyond this time. Detailed mesh-of-grind studies have indicated that 20 min of grinding yields optimum values of molybdenum and lead in the float product and hence this time was fixed for all subsequent experiments.

Preliminary experiments conducted to evaluate different inorganic depressants for galena have shown that satisfactory results are obtained only with sodium dichromate. Optimisation studies performed to arrive at the dosage of sodium dichromate have shown that the addition of 0.25 kg/t of sodium dichromate gives optimum results with respect of overall recovery and grade of molybdenum, copper and lead in the float and tailing fractions. In a similar manner, the optimum dosage of kerosene (collector for molybdenite) has been arrived at to be 0.8 kg/t, taking a holistic view of the grades and recoveries of the different metal values of interest. Based on the studies carried out with respect to optimisation of the mesh-of-grind, depressant and collector concentrations, it became apparent that a grade of about 0.8% Mo only could be achieved with over 80% recovery. The redeeming feature however was that over 90% of the feed could be rejected at the rougher flotation stage itself with a negligible loss of about 0.02% Mo in the tailings.

It was thus considered logical to further upgrade the Mo content by regrinding. An extensive flotation campaign was therefore mounted, adopting the following strategies:

(1) 1st stage regrinding and one cleaning,
(2) IInd stage regrinding and three cleanings,
(3) IIIrd stage regrinding and two cleanings.

Based on the first-stage regrinding tests it was found that by regrinding to 100% passing 106 microns, the Mo assay could be enhanced to over 32% from an initial value of about 0.1% in the feed. The enrichment ratio at this stage corresponds to about 340. After the second stage regrinding followed by three stages of cleaning, close to 75% recovery of Mo with an assay value of about 52% could be achieved, further enhancing the enrichment ratio to about 540. A few experiments were conducted using sodium cyanide during the second stage regrinding tests and it was found that the copper assay could be brought down to 0.3% from about 0.8%, without affecting the grade of lead and molybdenum. The results of the third-stage regrinding tests have highlighted that a final concentrate assaying about 55% molybdenum with over 70% recovery could be obtained. It is worthy to mention that the concentrate so produced meets the specification of metallurgical-grade molybdenite. The overall enrichment ratio obtained, commencing from a feed assaying 0.1% Mo, corresponds to about 580.

In order to explore the efficacy of organic depressants, which are more acceptable on environmental grounds, detailed flotation studies were carried out using dextrin with particular emphasis on galena depression. A series of experiments was carried out in an identical manner to those conducted using sodium dichromate. Here again, three stages of regrinding/cleaning tests were carried out, akin to those performed using sodium dichromate. A dextrin concentration of 0.01 kg/t was found to be an optimum value from the point of grade, wt% recovery and distribution of molybdenum, lead and copper in the cleaner concentrate.

It is noteworthy that after second stage regrinding followed by four stages of cleaning, the molybdenum assay value could be significantly improved from 16% to about 53% with over 70% recovery. Another notable feature is that the copper content in the concentrate is only about 0.2% even without the addition of sodium cyanide. The results of the third stage regrinding/cleaning tests have shown a marginal improvement in the molybdenum assay values without affecting the grade of copper and lead. On a comparative basis, it can be inferred that dex-

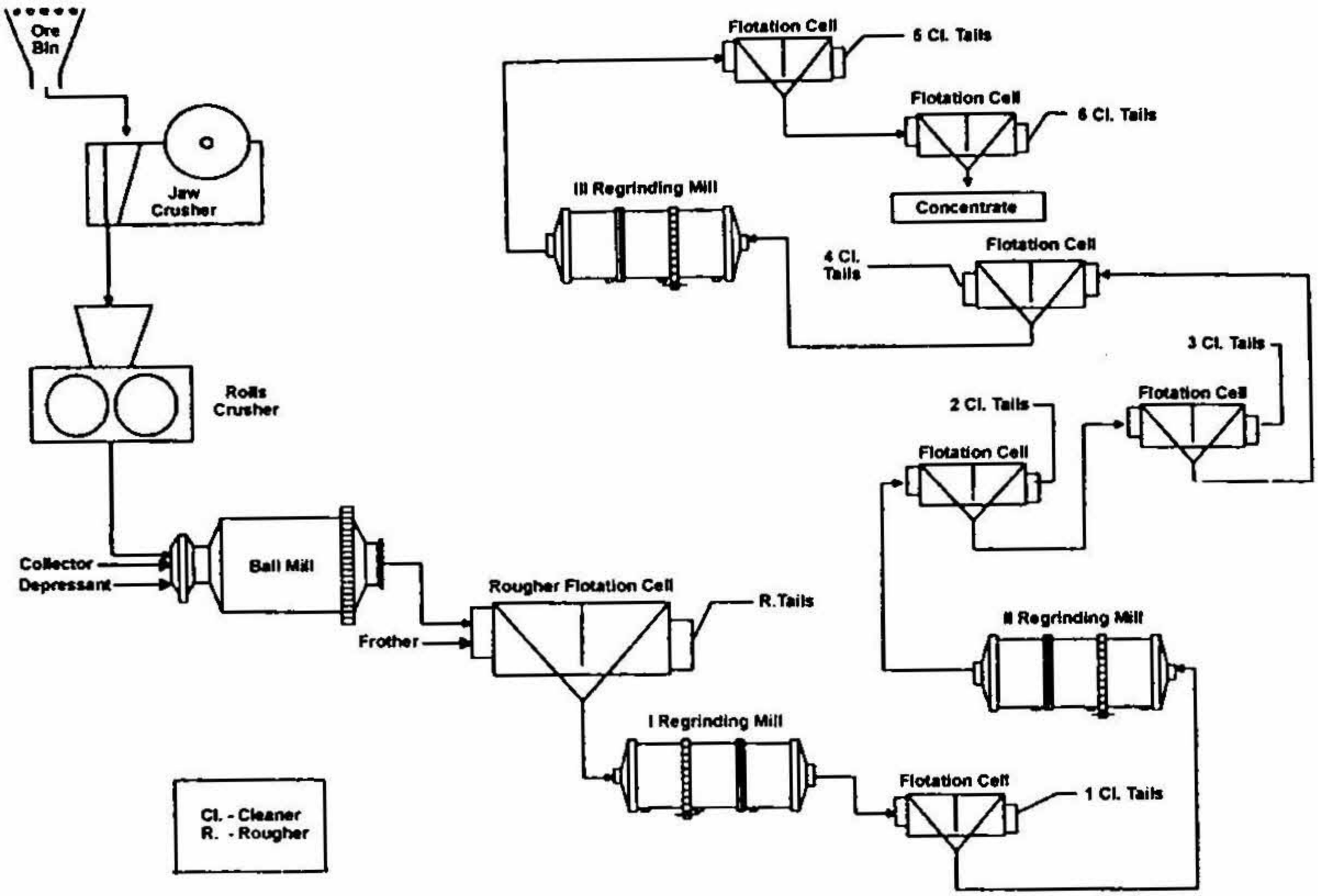

FIG. 1. Flowsheet for the beneficiation of molybdenite ore.

trin holds promise to be used as a potential substitute for inorganic depressants such as sodium dichromate and sodium cyanide. On the basis of extensive investigations carried out on the beneficiation of molybdenite ore, a comprehensive flowsheet has been developed (Fig. 1).

5. Conclusions

(1) Minerlogical studies have indicated that quartz and sericite are the predominant minerals followed by carbonates and feldspar. Among the sulphide minerals, pyrite is dominant with trace amounts of galena, sphalerite, chalocopyrite and molybdenite.

(2) Based on the various reagents evaluated, the combination involving kerosene and MIBC is found to yield optimum values of grade and recovery of molybdenum.

(3) Consequent to three stages of regrinding and two cleaning operations, the Mo grade could be enriched to about 55% with over 70% recovery. The concentrate so obtained meets the specifications for metallurgical-grade molybdenite.

References:

1. *Minerals Year Book*, Indian Bureau of Mines, Nagpur, 1996.

2. SHANMUGHAM, M., PALANISAMY, V., SINGANENJAM, S., GOPALA RAO, V. AND RAJU, K. *Rec. Geol. Surv. India*, 1995, **128**, (Part 5), 129.

INSTRUCTIONS TO AUTHORS

MANUSCRIPTS should be in English and written in a concise form. Three type-written double-spaced copies with one set of original Indian ink drawings and two sets of prints are to be submitted. The pages should be consecutively numbered and securely fastened.

TITLE PAGE should contain the following: (i) a brief title with suitable words for indexing; (ii) the names of the authors and the institution(s) where the work was carried out; (iii) a footnote with the present address of the authors, if different from (ii); (iv) a 75-word Abstract which summarizes the significant results of the communicated paper; (v) keywords for indexing and information retrieval; (vi) major discipline; and (vii) a running/short title.

TEXT should begin on page 2. It is preferable to break up the text into different sections, with suitable numbered headings, such as; 1. Introduction, 2. Experimental, 3. Theoretical analysis . . . , and 7. Conclusions. Acknowledgments should appear at the end of the paper, but before references.

REFERENCES should be indicated by Indian/Arabic numerals with superscript letters, *e.g.*, "Earlier Bose[6] has measured . . . ,". References should be typed in double space on a separate sheet in the order of their occurrence in the text and appended at the end of the paper. They should be given with full details as in the following examples:

3. RAMAKRISHNA NAIDU, G. AND NAIDU, P. R. — Isotopic exchange study of nickel xanthate in the presence of toluidines, *Proc. Indian Acad. Sci. A*, 1978, **87**, 443–446.

8. HINGDON, A. — *Engineering mechanics*, Vol. 1. Ch. 3, pp 79–104, 1968, Prentice-Hall.

9. RAMA MURTHY, K. — *Convergence of state distributions in multi-type Bellman-Harris and Crump-Mode-Jagers branching processes*, Ph.D. Thesis, Indian Institute of Science, Bangalore, India, 1978.

LENGTH of papers: Up to 25 pages (about 8,000 words) for full papers and 6 pages (2,000 words) for short communications.

TABLES should be included only when considered essential. They should be numbered consecutively with Roman numerals and typed on separate sheets. Every table should contain a descriptive title.

FIGURES should be drawn with Indian ink on good tracing paper. It is most important that the lines and letters are sufficiently bold to permit reduction to the *Journal* size. Captions should be typed on a separate sheet.

MATHEMATICAL SYMBOLS should be identified with pencil on the margins. Standard mathematical notations should be adhered to. Please distinguish between *kay* and *kappa*, *ell* and *one* and other similar symbols likely to cause confusion.

ABBREVIATIONS such as *e.g.*, *et al.*, and *i.e.*, can be used. If non-standard abbreviations or acronyms are used they should be explained where they appear first in the text.

GALLEY PROOFS will be sent to the authors for correction. They should be carefully scrutinized and returned within three days of receipt.

REPRINTS: Fifty reprints are supplied gratis. Additional reprints (up to 50) can be ordered while returning the corrected galley proof.

PAPERS received for publication are subjected to rigorous review process.

MANUSCRIPTS should be sent to the Editor, JOURNAL OF THE INDIAN INSTITUTE OF SCIENCE, C/O IISc Library, Bangalore 560 012, India. email: journal@library.iisc.ernet.in

Published by Prof. T. S. Ramamurthy, Executive Editor, *Journal of the Indian Institute of Science*, Bangalore 560 012; Typeset by Creative Literati Pvt. Ltd., Bangalore 560 043, Tel.-cum-Fax: 5454047, 5455808; Printed at Lotus Printers, Bangalore 560 044, Tel.: 3380167, Fax: 3357378.

Journal of the Indian Institute of Science
Bangalore 560 012, India

Volume 80 *September–October 2000* *Number 5*

Special Issue on Power Electronics at IISc–2

Contents